Long-term stable reduced models for hydraulic systems governed by Reynolds averaged Navier-Stokes equations

Lucas Reineking*, Kamil Sommer*,
Yogesh Parry Ravichandran**, Romuald Skoda**,
Martin Mönnigmann*

*Autom. Contr. & Syst. Theory, Ruhr-Universität Bochum, Germany.
**Hydraulic Fluid Machinery, Ruhr-Universität Bochum, Germany.
(e-mail: Lucas.Reineking@rub.de)

Abstract: Realtime reconstruction of flow fields is a prerequisite to precise condition monitoring of hydraulic plant components. Because models based on Navier-Stokes equations are usually too complex for a realtime use, reduced order models (ROMs) are a viable alternative. Specifically, ROMs based on proper orthogonal decomposition and Galerkin projection are attractive, because they result in small models comprising a few (in the order of ten) ordinary differential equations. However, ROMs of this type often turn out not to be stable even for stable points of operation of the real system and the original partial differential equation model. Stability properties can sometimes be improved by fitting the ROM to the original data obtained from finite-volume or similar simulations for the partial differential equation model. This is unsatisfactory because a ROM is first derived in a systematic manner and then altered a posteriori in an ad hoc fashion. We propose to use a Petrov-Galerkin projection instead, i.e., we retain the optimal truncated basis to span the simulation data space but optimize the basis used in the projection separately. We demonstrate this improves the stability properties of the ROM considerably for a centrifugal pump, which is modeled with the Reynolds averaged Navier-Stokes equations.

Keywords: reduced order model, Galerkin projection, Petrov-Galerkin projection, proper orthogonal decomposition, radial pump, incompressible Navier-Stokes equation

1. INTRODUCTION

CFD simulations are established tools for the analysis and optimization of hydraulic components such as pumps. CFD is too computationally intensive, however, for realtime applications such as condition monitoring. On the other hand, results obtained from CFD simulations can be used to derive reduced order models (ROMs), which can close the gap between high accuracy and fast evaluation. We apply projection-based model order reduction to data of flow fields computed with CFD. Specifically, we apply the method of snapshots in combination with proper orthogonal decomposition (POD) introduced by Sirovich (1987). Reductions of this type require two steps: The velocity field is represented as a linear combination of POD modes, and the dynamics governed by the incompressible Navier-Stokes equation are projected onto a finite-dimensional space. This results in a set of ordinary differential equations. We refer to the resulting ROM as POD-Galerkin-ROM.

POD-Galerkin-ROMs have been successfully derived both for reference problems, e.g., the Karman Vortex Street, and practical problems like airflow analysis (Deane et al., 1991; Bergmann and Cordier, 2008; John et al., 2010; Pyta and Abel, 2015). Some of these studies even considered parameter-dependent ROMs (Deane et al., 1991). Amsallem and Farhat (2008) proposed a manifold-based

adaption to variations in the free-stream Mach numbers for a reduced order model.

POD-Galerkin-ROMs after Sirovich (1987) have been reported not to work well for some problems modeled with the Navier-Stokes equations. As a remedy, these models are sometimes fitted to the original CFD simulation data by adjusting the coefficients in the ODE of the ROM. This has resulted in useful ROMs for complex problems including combustion and in combination with extended Kalman filters (Couplet et al., 2005; Pyta and Abel, 2015; Gunder et al., 2018).

We consider the velocity field in a fully resolved radial pump, which is shown in Figure 1. Note that the computational domain has a more complex shape than reference problems with Navier-Stokes equations such as the Karman Vortex Street. It is the purpose of the paper to compare the POD-Galerkin-ROMs, both before and after the ad hoc optimization described above, and a ROM that results from a more systematic optimization. We apply a manifold-based optimization approach to ROM that, in contrast to ad hoc optimizations, preserves the optimal basis for the expansion of the simulation data, and obtains an optimal basis for the projection step.

We briefly describe the CFD simulation and the model reduction steps in sections 2 and 3, respectively, as needed here. Subsection 3.3 states the alternative optimization
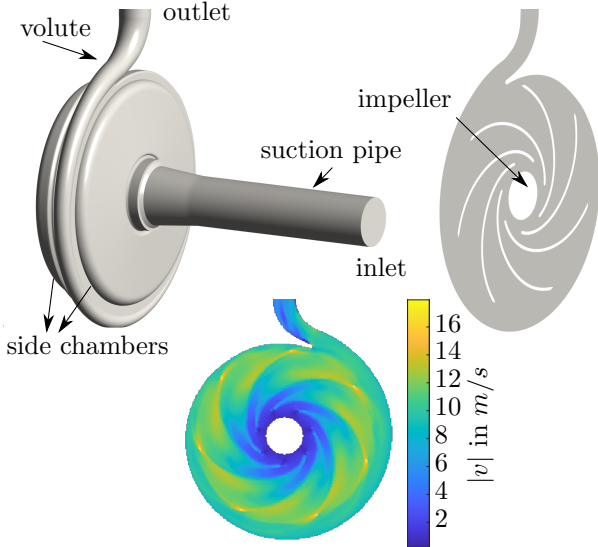
Fig. 1. Top: 3D Model of the pump (left) and the respective 2D axial section (right). The pressure pipe is hidden in this figure. Bottom: Velocity magnitude from CFD simulation with interpolated values inside the blades.

method. Results for the radial pump model from section 2 are given in section 4. Conclusions are stated in section 5.

2. MODEL SYSTEM

We consider a radial pump with a low specific speed ($n_s = 12\,1/\mathrm{min}$). We summarize the system and the numerical setup as needed here (for details, see Limbach and Skoda, 2017). The computational domain consists of an impeller with seven blades, a spiral volute, side chambers, and the suction and pressure pipe as shown in Figure 1. It is resolved with a body fitted, block-structured hexahedral grid with in total 1.8 million cells for the CFD simulation. This simulation combines the sliding grid approach with the conventional form of the Reynolds averaged Navier-Stokes equations

$$\frac{du}{dt} = -(u \cdot \nabla)u + (\nu + \nu_t)\Delta u - \nabla p, \qquad (1a)$$

$$\nabla \cdot u = 0, \qquad (1b)$$

where u, ν, ν_t and p denote the velocity, viscosity, eddy viscosity and pressure, respectively. We use the open-source computational mechanics software OPENFOAM (Weller et al., 1998) which proved reliable in similar studies (see Casimir et al., 2020 and citations therein). A Dirichlet inlet boundary condition is set for velocity ($u = 2.12\,ms^{-1}$) together with a Neumann (zero-gradient) condition for static pressure. At the outlet, Neumann boundary conditions are set for velocity (zero gradient) and a Dirichlet condition for static pressure. The impeller rotates at the nominal operation point such that the angular velocity is $\omega = 151.84 s^{-1}$.

We compute a 3D CFD solution for the described pump model and extract a 2D axial section of the flow field at the nominal operating point of the pump (see Figure 1). The flow field solution from the time-variant grids is interpolated onto a fixed, uniform cartesian grid. The moving impeller solid domain is treated as a fluid by interpolating values from the surrounding blade-wall adjacent flow fields (see Garcia, 2010; Wang et al., 2012). The simulated flow and pressure fields are recorded at $M = 52$ equidistant time points. We refer to a field at a fixed point in time as snapshot. The sampling time between snapshots corresponds to a rotation of the impeller by $1°$. The resulting $52°$ degrees captured with the snapshots correspond to a seventh of the full rotation of the impeller, which suffices to establish a periodic sequence of snapshots because the impeller has seven blades.

3. CONSTRUCTION OF ROM

3.1 Basic Techniques

We summarize two essential steps, proper orthogonal decomposition and the ROM construction by projection, as needed for the paper. Note that the singular value decomposition can be carried out efficiently with the method of snapshots (see, e.g., Volkwein, 2007).

Proper orthogonal decomposition The simulations described in section 2 yield the spatially and temporally resolved velocity $u : \Omega \times \mathbb{R} \to \mathbb{R}^d$ for every discrete time t_m, $m = 1, \ldots, M$ and gridpoint $x_n \in \mathbb{R}^d$, $n = 1, \ldots, N_{\mathrm{grid}}$, where $\Omega \subset \mathbb{R}^d$ is the spatial domain approximated by the gridpoints x_n.

We split velocities into a time-invariant mean $\bar{u}(x_n)$ and the time-variant part $\tilde{u}(x_n, t_m)$

$$u(x_n, t_m) = \bar{u}(x_n) + \tilde{u}(x_n, t_m).$$

and combine, for every t_m, velocities at all spatial grid points into column vectors

$$\left(\tilde{u}(x_1, t_m)^T, \ldots, \tilde{u}(x_n, t_m)^T \right)^T. \qquad (2)$$

Collecting these column vectors in the order $m = 1, \ldots, M$ results in $U \in \mathbb{R}^{N \times M}$, which we refer to as the snapshot matrix. Note that $N = d\,N_{\mathrm{grid}} = 2N_{\mathrm{grid}}$, since all velocity fields are two-dimensional throughout the paper.

Applying a singular value decomposition to U yields $U = \Phi^{\mathrm{svd}}\Sigma V^T$, where the columns of Φ^{svd} are an orthonormal basis of the column space of U. We denote the i-th column of Φ^{svd} by Φ_i^{svd} and refer to it as the i-th mode.

It is the central idea of proper orthogonal decomposition to select the $R \ll M$ columns with the largest singular values in Σ as an approximate basis for the simulation data, i.e., for the column space of U. Assuming $\bar{R}$ singular values $\sigma_i > 0$ exist and are ordered such that $\sigma_1^2 \geq \sigma_2^2 \geq \ldots$, the number $\mathcal{E}_u(R)$ defined by

$$\mathcal{E}_u(R) = \sum_{i=1}^{R} \sigma_i^2 / \sum_{i=1}^{\bar{R}} \sigma_i^2 \qquad (3)$$

is a measure for the approximation quality of the truncated basis. This implies any velocity vector (2) in U, or any linear combination of the columns (2), can be approximated with the columns Φ_i^{svd}, $i = 1, \ldots, R$, to an error controllable with $\mathcal{E}(R)$. We can split Φ_i^{svd} into components

$$\Phi_i^{\mathrm{svd}} = \left(\phi_i^{\mathrm{svd}}(x_1)^T, \ldots, \phi_i^{\mathrm{svd}}(x_n)^T \right)^T \in \mathbb{R}^N \qquad (4)$$

that belong to the same spatial grid points as those in (2). Just as the Φ_i^{svd} form a truncated basis for the column space of U, the $\phi_i^{\mathrm{svd}}(x_n)$ defined by (4) can be used to expand any $\tilde{u}(x_n, t_m)$. This implies there exist, for any $\tilde{u}(x_n, t_m)$, coefficients $a(t_m)$ such that

$$\tilde{u}(x_n, t_m) \approx \sum_{i=1}^{R} a_i(t_m)\phi_i^{\mathrm{svd}}(x_n). \qquad (5)$$

The coefficients $a_i(t_m)$ can be constructed with the methods described in the second part of this section and in Section 3. Note that adding the time-invariant mean yields

$$u(x_n, t_m) \approx \bar{u}(x_n) + \sum_{i=1}^{R} \phi_i^{\mathrm{svd}}(x_n) \cdot a_i(t_m). \quad (6)$$

Examples of a mode Φ_i^{svd} and coefficients a_i are shown in Figs. 3 and 5, respectively.

ROM construction by projection The second step, the construction of the reduced order model (ROM), can be split into two substeps again. First, u is approximated in the Navier-Stokes equations by substituting (6) into (1). The resulting approximate equations are then projected onto the basis vectors (4), or basis vectors optimized for this purpose described below. We denote the basis vectors used in the second step by

$$\Psi_i = \left(\psi_i(x_1)^T, \ldots, \psi_i(x_n)^T \right)^T \in \mathbb{R}^N, \quad (7)$$

$i = 1, \ldots, R$, and collect them in $\Psi \in \mathbb{R}^{N \times R}$ to permit this generalization. The projection requires the scalar product

$$\langle f, g \rangle = \sum_{n=1}^{N} f(x_n) \cdot g(x_n), \quad (8)$$

for any $f, g : \Omega \to \mathbb{R}^d$. The two substeps result in a set of R ordinary differential equations

$$\sum_{i=1}^{R} W_{ki} \frac{da_i(t)}{dt} = \sum_{i=1}^{R} \sum_{l=1}^{R} a_i(t) a_l(t) Q_{kil}$$
$$+ \sum_{i=1}^{R} a_i(t) L_{ki} + C_k =: f_k(a(t)) \quad (9a)$$

$k = 1, \ldots, R$, where $f_k(a)$ is used as an abbreviation and

$$\begin{aligned} W_{ki} &= + \langle \psi_k, \phi_i^{\mathrm{svd}} \rangle, \quad Q_{kil} = -\langle \psi_k, (\phi_i^{\mathrm{svd}} \cdot \nabla) \phi_l^{\mathrm{svd}} \rangle, \\ L_{ki} &= + \langle \psi_k, \nu \Delta \phi_i^{\mathrm{svd}} \rangle - \langle \psi_k, (\bar{u} \cdot \nabla) \phi_i^{\mathrm{svd}}) \rangle \\ &\quad - \langle \psi_k, (\phi_i^{\mathrm{svd}} \cdot \nabla) \bar{u} \rangle, \\ C_k &= - \langle \psi_k, (\bar{u} \cdot \nabla) \bar{u} \rangle + \langle \psi_k, \nu \Delta \bar{u} \rangle, \end{aligned} \quad (9b)$$

$i, l = 1, \ldots, R$. The differential operators in (9b) are used to avoid a too cumbersome notation here. They need to be replaced by discrete approximations (see, e.g., John et al., 2010). The pressure term is usually neglected (see, e.g., John et al., 2010). As the zero divergence of the velocity is already guaranteed in the CFD simulation, the continuity equation (1b) also holds for (6) within the approximation controlled with $\mathcal{E}(R)$ (see, e.g., Deane et al., 1991; John et al., 2010).

The simplest choice for the modes Ψ_k are the modes Φ_k^{svd}. The projection is often referred to as Galerkin-projection in this case. Because the Φ_k^{svd} are orthogonal and normalized by construction, they yield a particularly simple mass matrix

$$W_{ki} = \langle \phi_k^{\mathrm{svd}}, \phi_i^{\mathrm{svd}} \rangle = \delta_{ki} \quad (10)$$

with Kronecker's δ_{ki}. This results in ODEs (9a) with particularly simple left-hand sides

$$\frac{da_k(t)}{dt} = f_k(a(t)), \ k = 1, \ldots R. \quad (11)$$

Because the projection with the particular choice $\Phi_k = \Phi_k^{\mathrm{svd}}$ is usually called Galerkin projection, we refer to the ROM (11) as POD-Galerkin-ROM. The flow field $u(x_n, t_m)$ can be reconstructed by solving (9a) with the initial condition $a_k(0) = \langle \tilde{u}(\cdot, 0), \phi_k \rangle$, $k = 1, \ldots, R$ and by evaluating (6).

3.2 Optimization of ROM by Simulation Data Fitting

It is common practise to postprocess the reduced order model (11) by optimizing its coefficients (9b) such that $a(t)$ fit the original simulation data as good as possible (see, e.g., Pyta and Abel, 2015; Couplet et al., 2005). This approach is described below because it is needed for the purpose of comparison. Section 3.3 then introduces an alternative optimization method that exploits the nonlinear geometric structure of the problem at hand. We claim the approach described in section 3.3 to be superior and show this claim holds for the example treated here in section 4. The standard optimization approach can be carried out as follows. Calculating the scalar product with ϕ_k^{svd} on both sides of (5) yields

$$\langle \Phi_k^{\mathrm{svd}}, \tilde{u}(\cdot, t_m) \rangle \approx a_k(t_m), \quad (12)$$

for all k and m, where the right-hand side results with (10). The left-hand side of (12), which we abbreviate by $a_k^{\mathrm{svd}}(t_m)$, is the best approximation that can be obtained with the truncated basis. It is therefore obvious to solve the optimization problem

$$\min_{Q_{kil}, L_{ki} C_k} \sum_{k=1}^{R} \sum_{m=1}^{M} (a_k^{\mathrm{svd}}(t_m) - a_k(t_m))^2 \text{ subj. to } (11) \quad (13)$$

to determine the values for the coefficients Q_{kil}, L_{ki}, C_k for the ROM (9a) that result in the best approximation of $a_k^{\mathrm{svd}}(t_m)$ by (9a). We denote the resulting values by Q_{kil}^{fit}, L_{kil}^{fit} and C_k^{fit} and the coefficients that result with these parameters by $a^{\mathrm{fit}}(t)$.

3.3 Optimization of ROM on Grassmann manifold

The optimization (13) essentially fits the reduced model to the original simulation data. Arguably, it is unsatisfactory to first derive a reduced model systematically, and then to adjust its coefficients in an ad hoc fashion. In this section, we show that the basis vectors (7) and their use in (9) provide the degrees of freedom for a systematic optimization. Replacing the fit (13) by this systematic optimization results in a reduced model with superior stability properties in section 4.

The reduced order model from section 3 uses the POD-modes Φ_i^{svd} introduced in (4) twice,

(i) as a basis for the flow fields (see (5), (6)), and
(ii) in the projections (9b) that yield the coefficients of the reduced order model (9a).

While the modes Φ_i^{svd} are known to be optimal for (i) (see, e.g., Volkwein, 2007, theorem 2.1), they are not in general optimal for (ii). Methods that use the modes Φ_i^{svd} for both expansion and projection, i.e., for both (i) and (ii), are collectively called Galerkin methods. Methods that use the modes Φ_i^{svd} only for (i) but permit Ψ_i introduced in (7) to differ from Φ^{svd} are often called Petrov-Galerkin methods (see, e.g., Fletcher, 1984, sec. 7.2). Petrov-Galerkin methods like balanced truncation are established for linear systems (Benner et al., 2015, sec. 2.2). Their application to non-linear systems is subject to ongoing research (see, e.g., Berner and Mönnigmann, 2021).

We explain how to determine the optimal Ψ_i for (ii) in the remainder of the section. Let $\Psi \in \mathbb{R}^{N \times R}$ be the matrix with columns Ψ_i introduced in (7). Let $\Phi \in \mathbb{R}^{N \times R}$ be the matrix that contains the first R columns of $\Phi^{\mathrm{svd}} \in \mathbb{R}^{N \times N}$
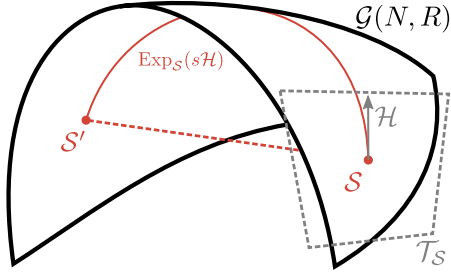
Fig. 2. Illustration of the Grassmann manifold $\mathcal{G}(N, R)$.

introduced below (2). Recall these first R columns contain the information used for the expansion of the flow field (6). Furthermore, recall the functions $a_i(t)$ that solve the reduced order model (9) for a given initial condition depend on Ψ, because the ψ_i appear in (9b). We write $a_i(t; \Psi)$ to make this dependence clear throughout this section.

Finding the optimal matrix $\Psi \in \mathbb{R}^{N \times R}$ provides $N \times R$ degrees of freedom to the optimization at first sight. This number can be reduced by exploiting the properties of the set of Ψ as follows. Finding the optimal $\Psi \in \mathbb{R}^{N \times R}$ is equivalent to finding a specific R-dimensional subspace of $\mathbb{R}^N$ spanned by the columns Ψ_i. The set of all R-dimensional subspaces of $\mathbb{R}^N$ is itself not a linear space, but a manifold, which we denote $\mathcal{G}(N, R)$ and which is a Grassmann manifold. From a theoretical point of view, any element $\mathcal{P}$ of $\mathcal{G}(N, R)$ is an equivalence class of orthogonal matrices in $\mathbb{R}^{N \times R}$, where two matrices are equivalent if their columns span the same R-dimensional subspace. This implies $\dim \mathcal{G}(N, R) = R(N - R)$ (see, e.g., Edelman et al., 1998), thus only $R(N - R)$ degrees of freedom exist in the optimization over all $\Psi \in \mathcal{G}(N, R)$. We represent an element of $\mathcal{G}(N, R)$ by an arbitrary orthonormal matrix from the equivalence class in the numerical optimization.

Having introduced $\mathcal{G}(N, R)$, the optimization problem can be stated. It reads

$$\min_{\Psi} \sum_{k=1}^{R} \sum_{m=1}^{M} (a_k^{\text{svd}}(t_m) - a_k(t_m; \Psi))^2 \quad (14)$$

subject to range $\Psi \in \mathcal{G}(N, R)$ and (9)

Let the optimal solution be denoted by Ψ^{GCG}, the coefficients (9b) that result with Ψ^{GCG} by Q_{kil}^{GCG} etc., and the coefficients that result with the ROM (9a) with these coefficients by $a^{\text{GCG}}(t)$. The label GCG is short for Grassmann conjugate gradient.

We summarize the most important aspects of solving (14) in the remainder of this section. In order to restrict the optimization to the $R(N - R)$ degrees of freedom explained above, we have to restrict it to Ψ that span subspaces in the manifold $\mathcal{G}(N, R)$. This is sketched in Fig. 2, where $\mathcal{S} =$ range Ψ and $\mathcal{S}' =$ range Ψ'. Instead of linear combinations of Ψ and Ψ' (dashed red line in Fig. 2), which are not in general elements of $\mathcal{G}(N, R)$, we need to consider geodesics (solid red line). Geodesics originating from $\mathcal{S} \in \mathcal{G}(N, R)$ can be parametrized with a single real parameter with the exponential map $\text{Exp}_{\mathcal{S}}(\cdot)$, which can be introduced as follows (Edelman et al., 1998, sec. 2.5). A geodesic emanating at $\mathcal{S}$ is uniquely defined by its tangent $\mathcal{H}$ at $\mathcal{S}$. Given a matrix representation $H \in \mathbb{R}^{N \times R}$ for $\mathcal{H}$, the exponential map can be defined by

$$\text{Exp}_{\mathcal{S}}(s\mathcal{H}) = \Psi \hat{V} \cos(\hat{\Sigma} s) \hat{V}^T + \hat{U} \sin(\hat{\Sigma} s) \hat{V} \quad (15)$$

Data: Given $\Psi^{(0)} = \Phi$ such that $\Psi^{(0)T} \Psi^{(0)} = I$, ε_{opt}
Result: Orthogonal basis $\Psi^{(j)}$ representing a test space minimizing F
compute initial gradient $G^{(0)} = \frac{\partial F}{\partial \mathcal{P}}$ according to (16)
set $j = 0$ and initial search direction to $H^{(j)} = -G^{(0)}$
while $F(\Psi^{(j)})/\sum_{l=R+1}^{M} \sigma_l^2 > \varepsilon_{\text{opt}}$ **do**

    Minimize $F(\Psi^{(j)}(s))$ via a line search along the geodesic, using the exponential map in (15) with direction $H^{(j)}$
    set $\Psi^{(j+1)}$ according to (A.1)
    compute new gradient $G^{(j+1)}$ according to (16)
    calculate parallel transportations $H^{(j)\|}$ acc. to (A.2) and $G^{(j)\|}$ accordingly
    determine conjugacy factor γ_j according to (A.3)
    compute the new search direction
    $H^{(j+1)} = -G^{(j+1)} + \gamma^{(j)} H^{(j)\|}$
    reset $H^{(j+1)} = -G^{(j+1)}$ if $j + 1 \equiv 0 \mod R(N - R)$
    set $H^{(j)} = H^{(j+1)}$, $G^{(j)} = G^{(j+1)}$, $\Psi^{(j)} = \Psi^{(j+1)}$ and $j = j + 1$
end

Algorithm 1. Conjugate gradient method on Grassmann manifold following Edelman et al. (1998, sec. 3.3).
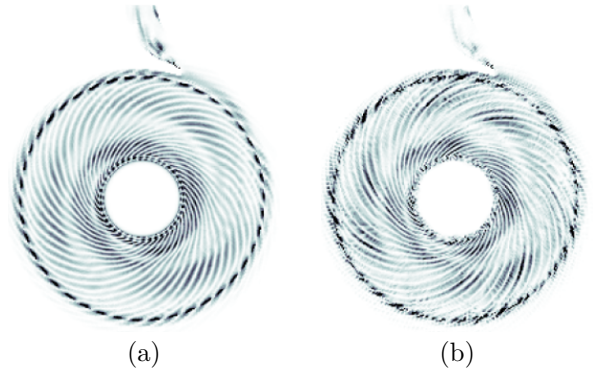

(a)	(b)

Fig. 3. Magnitude of mode $\phi_5(x_n)$ from POD (a) and of mode $\psi_5(x_n)$ from of the solution to (14) (b).

where $H = \hat{U} \hat{\Sigma} \hat{V}^T$ is a thin singular value decomposition and $s \in [0, 1]$ is a scalar parameter. Note that for $s = 0$ the exponential map $\text{Exp}_{\mathcal{S}}(0)$ yields $\mathcal{S}$.

The parametrization (15) is needed to carry out line searches in the optimization along geodesics. The second important ingredient to the optimization algorithm are derivatives for determining descent directions. Let F refer to the cost functional in (14). Then the derivative with respect to a subspace $\mathcal{S}$ can be determined with

$$\frac{\partial F}{\partial \mathcal{S}} = \frac{\partial F}{\partial \Psi} - \Psi \Psi^T \frac{\partial F}{\partial \Psi} \quad (16)$$

where $\frac{\partial F}{\partial \Psi}$ denotes the componentwise partial derivative of F with respect to its basis representation Ψ. The derivative (16) is a tangent to the manifold $\mathcal{G}(N, R)$ at $\mathcal{S}$, hence, the parametrization (15) is used to map the derivative onto the manifold $\mathcal{G}(N, R)$, i.e., the parametrization (15) allows for moving in the descent direction on the manifold $\mathcal{G}(N, R)$.

The combination of a line search in (15) with the derivatives (16) then permits solving (14) with a conjugate-gradient method following Edelman et al. (1998, sec. 3.3). This results in Algorithm 1. The conjugacy factor γ_j is computed with the method of Pollak-Ribiere (Edelman et al., 1998, sec. 2.6). Since this method originally applies to linear spaces, it needs to be extended for use with $\mathcal{G}(N, R)$. A brief summary of the required steps is given in appendix A.
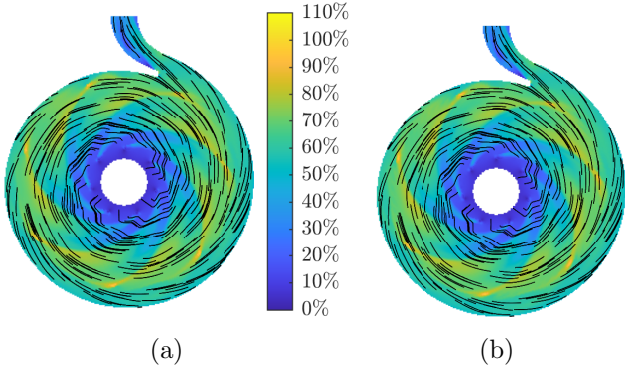
Fig. 4. Velocity fields at $t = t_0 + T/2$: (a) magnitude, (b) magnitude recovered from coefficients $a^{\mathrm{GCG}}(t)$. Both fields are scaled to the tangential speed of the impeller outer radius. Solid black lines are streamlines.

Table 1. Parameters for reduction and optimization

Quantity		value
number of snapshots	M	52
number of cells	N_{grid}	36179
number of modes	R	16
dimension of velocity	d	2
dimension of modes	N	72385
approx. quality	$\mathcal{E}_u$	0.9884
Grassmann manifold	$\mathcal{G}(N, R)$	$\mathcal{G}(72358, 16)$
dimensionless conv. crit.	$\varepsilon_{\mathrm{opt}}$	0.0025

4. RESULTS FOR THE EXAMPLE

We apply the optimization methods introduced in sections 3.2 and 3.3 to the 2D velocity field in an axial section of a radial pump introduced in section 2 and analyze the numerical stability of the resulting reduced order models with numerical experiments. The axial section of the pump is modeled with $N_{\mathrm{grid}} = 36179$ uniform cells with $d = 2$ velocity components in each cell. The POD modes are generated from $M = 52$ velocity snapshots describing a period T, and we truncate the system to $R = 16$ modes which results in $\mathcal{E}_u(R) \approx 99\%$. The resulting time coefficients $a^{\mathrm{svd}}(t_m)$, $m = 1, \ldots, M$ are used in the optimization problems (13) and (15). Since $N = N_{\mathrm{grid}}d = 72358$, the relevant Grassmann manifold is $\mathcal{G}(72358, 16)$. Obviously, great care must be taken for the implementation of the manifold-based algorithms due to their large size. Both optimization algorithms are terminated when the stopping criterion $\varepsilon_{\mathrm{opt}} = 0.0025$ is reached. The parameters are summarized in table 1.

We evaluate the two reduced order models that result with the optimization methods for three time periods T and compare time coefficients to a^{svd} in Fig. 5. A good agreement of $a^{\mathrm{GCG}}(t)$ and $a^{\mathrm{svd}}(t)$ is evident from the figure. In contrast, the time coefficients $a^{\mathrm{fit}}(t)$ obtained with the fitting algorithm from subsection 3.2 differ increasingly in the second period and are not useful anymore in the third period.

We note that the model that results with the method introduced in section 3.3 results in a better approximation even though the changes made to the modes Φ_i to obtain the optimal Ψ_i in (15) are subtle. This is illustrated in Fig. 3.

Figure 4 shows the a velocity snapshot and the velocity field reconstructed from the coefficients $a^{\mathrm{GCG}}(t)$.

As expected of the reconstruction $\hat{u}(x_n, t) = \bar{u}(x_n) + \sum_{i=1}^{R} \phi_i(x_n) \cdot a_i^{\mathrm{CGC}}(t)$, the difference between both velocity fields is small on average, i.e., it is below 1% in root mean square error, despite some isolated larger errors around the blade tips. The difference of the velocity fields mostly originates from the truncation in (3). The optimization method in section 3.3 enforces the additional error of the ROM to be $\varepsilon_{\mathrm{opt}} = 0.0025$, i.e., an error that is three orders of magnitudes smaller than the error from the truncation. It is an obvious question to ask how the reduced order models perform for longer time spans. The ROM obtained by least-squares fitting prohibits evaluations for longer time periods and is very sensitive to even small perturbation in the initial conditions. In contrast, the reduced order model obtained in section 3.3 converges to a stable limit cycle (see Fig. 6), and this limit cycle is close to the limit cycle that results for the original simulation data, i.e., for $a^{\mathrm{svd}}(t)$. Our numerical experiments indicate that the reduced order model from section 3.3 tolerates perturbations in the initial conditions of 10%. The system is attracted to the same limit cycle after such perturbations. However, a further decrease of $\varepsilon_{\mathrm{opt}}$, e.g., $\varepsilon_{\mathrm{opt}} = 0.0005$, yields an eventually unstable POD-Petrov-Galerkin-ROM. The resulting ROM shows still far better long-term behavior than the POD-Galerkin-ROM in that it results in bounded coefficients for approximately $250T$, but misses a stable limit cycle.

5. CONCLUSION AND OUTLOOK

We demonstrated that long-term stable reduced order models can be obtained for hydraulic systems governed by the Reynolds averaged Navier-Stokes equations. Established methods do not result in stable reduced order models for the example treated here. We propose to replace a popular a posteriori fit of the reduced order model with a more systematic optimization. In contrast to the a posteriori fit, the proposed method leaves the truncated basis, which results from a proper orthogonal decomposition, unaltered, and optimizes the projection basis used for generating the ODE. In contrast to both the ROM with and without a posteriori fitting, the new ROM is long-term stable.

Furthermore, the proposed method is compatible with parameter-dependent reductions such as proposed by Amsallem and Farhat (2008). Future work will address the combination of the method proposed here with parameter-dependent reductions. Moreover, future work will address the extension to the full 3d pump model.

REFERENCES

Amsallem, D. and Farhat, C. (2008). Interpolation method for adapting reduced-order models and application to aeroelasticity. *AIAA Journal*, 47(7), 1803–1813.

Benner, P., Gugercin, S., and Willcox, K. (2015). A survey of projection-based model reduction methods for parametric dynamical systems. *SIAM Review*, 57(4), 483–531.
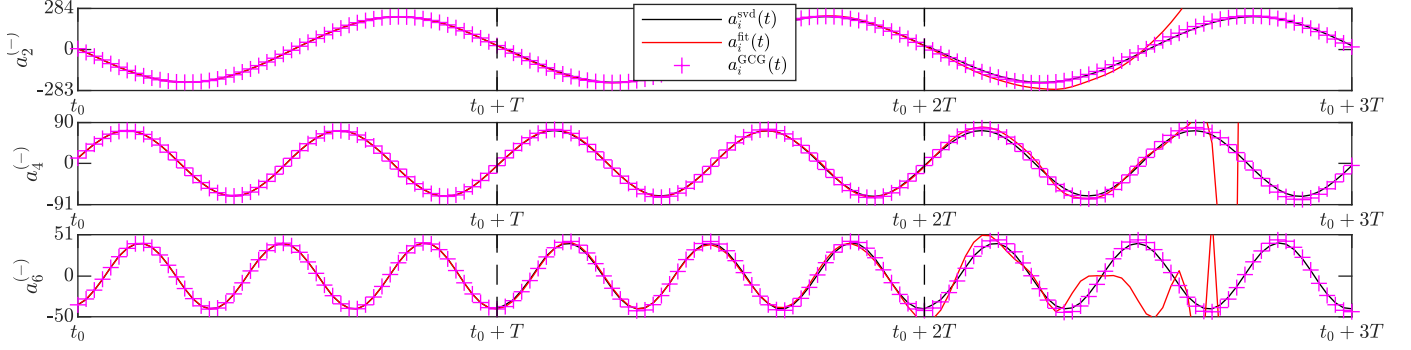
Fig. 5. ROM coeff. $a_i^{\text{fit}}(t)$ and $a_i^{\text{GCG}}(t)$ for modes 2, 4 and 6 of the two opt. methods compared to SVD coeff. $a_i^{\text{svd}}(t)$.
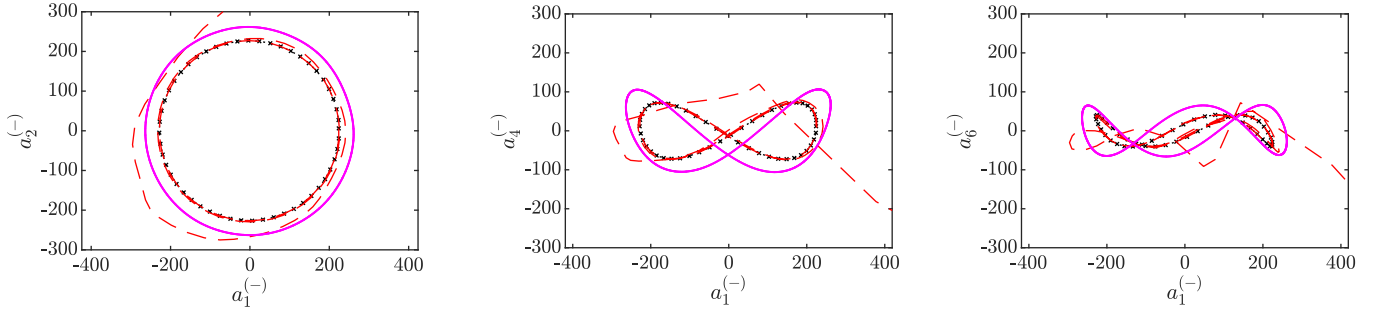

Fig. 6. Orbits of $a_i^{\text{svd}}(t_m)$ marked with black crosses, $a_i^{\text{fit}}(t)$ for three periods T marked with the red dashed line, limit cycle of POD-Petrov-Galerkin ROM marked with magenta line. Both ROMs start at the POD coefficients.

Bergmann, M. and Cordier, L. (2008). Optimal control of the cylinder wake in the laminar regime by Trust-Region methods and POD Reduced-Order Models. *J. Comput. Phys.*, 8, 7813–7840.

Berner, M.O. and Mönnigmann, M. (2021). Comparison of two model reduction approaches of an industrial drying process. *at-Automatisierungstechnik*, 69(8), 667–682.

Casimir, N., Zhu, X., Hundshagen, M., Ludwig, G., and Skoda, R. (2020). Numerical study of rotor-stator interaction of a centrifugal pump at part load with special emphasis on unsteady blade load. *J. Fluids Eng. Trans. ASME*, 142(8), 30.

Couplet, M., Basdevant, C., and Sagaut, P. (2005). Calibrated reduced-order POD-Galerkin system for fluid flow modelling. *J. Comput. Phys.*, 207, 192–220.

Deane, A., Kevrekidis, I.G., Karniadakis, G., and Orszag, S.A. (1991). Lowdimensional models for complex geometry flows: Application to grooved channels and circular cylinders. *Physics of Fluids*, 3, 2337–2354.

Edelman, A., Arias, T., and Smith, S. (1998). The geometry of algorithms with orthogonality constraints. *SIAM J. Matrix Anal. Appl.*, 20(2), 303–353.

Fletcher, C.A.J. (1984). *Computational Galerkin Methods*. Springer Series in Computational Physics. Springer-Verlag New York.

Garcia, D. (2010). Robust smoothing of gridded data in one and higher dimensions with missing values. *Comput. Stat. Data Anal.*, 54(4), 1167–1178.

Gunder, T., Sehlinger, A., Skoda, R., and Mönnigmann, M. (2018). Sensor placement for reduced-order model-based observers in hydraulic fluid machinery. *IFAC-Pap. Online*, 51(13), 414 – 419.

John, T., Guay, M., Hariharan, N., and Naranayan, S. (2010). POD-based observer for estimation in Navier-Stokes flow. *Comput. Chem. Eng.*, 34(6), 965 – 975.

Limbach, P. and Skoda, R. (2017). Numerical and experimental analysis of cavitating flow in a low specific speed centrifugal pump with different surface roughness. *J. Fluids Eng. ASME*, 139(10): 101201 (8 pages).

Nocedal, J. and Wright, S.J. (1999). *Numerical Optimization*. Springer series in Operations Research. Springer-Verlag New York.

Pyta, L. and Abel, D. (2015). Model based control of the incompressible navier-stokes-equations using interpolatory model reduction. In *Proc. 54th IEEE Conf. Decis. Control*, 7316–7321.

Sirovich, L. (1987). Turbulence and the Dynamics of coherent Structures. Part I-III. *Q. Appl. Math.*, 45(3), 561–571.

Volkwein, S. (2007). Proper orthogonal decomposition: Applications in optimization and control. *INRIA Num. Anal. Summ. Sch.*

Wang, G., Garcia, D., Liu, Y., de Jeu, R., and Dolman, A.J. (2012). A three-dimensional gap filling method for large geophysical datasets: Application to global satellite soil moisture observations. *Environmental Modelling & Software*, 30, 139–142.

Weller, H.G., Tabor, G., Jasak, H., and Fureby, C. (1998). A tensorial approach to computational continuum mechanics using object-oriented techniques. *Computers in Physics*, 12(6), 620–631.

Appendix A. CALCULATION OF $\gamma^{(j)}$

Let the upper index j count iterations as in Alg. 1. Assume there exists a local minimum of $F(\Psi^{(j)}(s))$ at $s = s_{\min}$ on the geodesic given by the search direction $H^{(j)}$. Let

$$\Psi^{(j+1)} = \text{Exp}_{\text{range } \Psi^{(j)}}\left(s_{\min}H^{(j)}\right). \quad (A.1)$$

Any matrix representation, such as $G^{(j)}$, of a tangent vector given in the tangent space at range $\Psi^{(j)}$ can be parallel transported along the geodesic to the local minimum spanned by $\Psi^{(j+1)}$. This results in $G^{(j)\|} =$

$$G^{(j)} - \left(\Psi^{(j)}\hat{V}\sin(\hat{\Sigma}s_{\min}) + \hat{U}\left(I - \cos(\hat{\Sigma}s_{\min})\right)\right)\hat{U}^T G^{(j)} \quad (A.2)$$

where $\hat{U}\hat{\Sigma}\hat{V}^T$ is as in section 3.3. The conjugacy factor γ_j after Pollak-Ribiere then reads

$$\gamma^{(j)} = \frac{\langle G^{(j+1)} - G^{(j)\|}, G^{(j+1)}\rangle_e}{\langle G^{(j)}, G^{(j)}\rangle_e} \quad (A.3)$$

where $\langle\cdot,\cdot\rangle_e$ denotes the Frobenius inner product. We refer to (Edelman et al., 1998, sec. 2.5) for parallel transport and to (Nocedal and Wright, 1999, sec. 5.2) for the conjugate gradient method.